Design, Modeling and Control of a Solar-Powered Quadcopter

9 authors, including:

Nathaniel Kingry
Collins Aerospace
9 PUBLICATIONS **161** CITATIONS

SEE PROFILE

Yue Zu
Iowa State University
13 PUBLICATIONS **101** CITATIONS

SEE PROFILE

Yuchen Wang
The Ohio State University
12 PUBLICATIONS **101** CITATIONS

SEE PROFILE

Yusuke Katagiri
Nagoya University
4 PUBLICATIONS **61** CITATIONS

SEE PROFILE

Design, Modeling and Control of a Solar-Powered Quadcopter

9 authors, including:

Nathaniel Kingry
Collins Aerospace
9 PUBLICATIONS **149** CITATIONS

Yuchen Wang
The Ohio State University
10 PUBLICATIONS **74** CITATIONS

Yue Zu
Iowa State University
13 PUBLICATIONS **94** CITATIONS

Yusuke Katagiri
Nagoya University
4 PUBLICATIONS **55** CITATIONS

Design, Modeling and Control of a Solar-Powered Quadcopter

Nathaniel Kingry, Logan Towers, Yen-Chen Liu, Yue Zu,
Yuchen Wang, Briana Staheli, Yusuke Katagiri, Samuel Cook, and Ran Dai

Abstract— This paper presents the design, modeling, control, and experimental test of a solar-powered quadcopter to allow for long-endurance missions. We first present the design of a large-scale quadcopter that incorporates solar energy harvesting capabilities. Based on the design results, we built the dynamical model of the customized quadcopter with analysis of the aerodynamic influence. A feedback control system is developed for the solar-powered quadcopter that takes into account the wind disturbance and is verified in virtual simulation examples. All parameters used in the modeling and simulations are based on a developed prototype of the solar-powered quadcopter. Flight tests with the prototype are presented to validate the theoretical basis of the solar-powered quadcopter.

Index Terms— Solar Energy, Quadcopter, System Design, Vehicle Control

I. Introduction

Quadcopters, as opposed to fixed-wing aerial vehicles, are classified as a type of unmanned aerial vehicle (UAVs) and have been used in many applications, such as environmental monitoring, communication, delivery service, etc., due to their greater maneuverability, hovering capability, and low cost [1], [2]. While quadcopters have their obvious advantages in a wide area of applications, existing quadcopter platforms are subject to limited flight duration. A small to medium sized quadcopter, e.g., DJI Phantom 4 PRO, can barely achieve 30 minutes flight time [3]. Although new techniques for autonomous battery swapping has been developed to resume the UAV flight, it still has flight duration limitations and drastically reduces the mobility of UAVs due to frequent recalls of battery swapping [4]. In this paper, we investigate the feasibility of integrating renewable energy harvesting capabilities into a quadcopter to allow for long-endurance missions with payload requirements.

Attempts to extend an aerial vehicle's operational time have, in large part, focused on the selection of efficient components [5], [6], energy optimized system design, and the use of power-efficient path planning [7]. For example, Verbeke et al. demonstrated a modified configuration for narrow corridors, which leads to potentially 60% increased endurance [8]. More recently, Pang et al. incorporated variable-pitch rotors into a gasoline-engine to extend flight duration

approaching 2 to 3 hours [9]. Other researchers proposed using hybrid energy sources, such as integrating rotational energy harvesting, laser power beaming, and solar energy, to increase flight durations [10]–[12].

Besides flight duration, the payload capability plays an important role when evaluating the system performance of a quadcopter. Early attempts to develop a quadcopter capable of lifting a large payload included the HoverBot [13], which was a 6 kg quadcopter designed from four hobby helicopters. Later attempts by Cornell University [14] developed the Cornell's Autonomous Flying Vehicle (AFV) based on commercially available components, which leads to a custom-designed AFV of 6.2 kg weight and 1.8 kg payload. Another work in [15] developed a 4 kg quadrotor with a 1 kg payload by addressing key design considerations that are essential for the construction of heavy quadcopters.

There is extensive investigation of efficient control strategies that contribute to greater robustness and maneuverability of a quadcopter, especially under external disturbances, such as proportional-integral-derivative (PID) control, model predictive control [16], and PID-LQR integrated control [17]. Although small-scale solar-powered quadcopters have been developed [12], [18], to our knowledge, there is no existing work addressing modeling and control of a solar-powered quadcopter. Therefore, when using an existing autopilot to control the trajectory of a large-scale solar-powered quadcopter, further stability analysis need to be investigated to design a tuned PID controller for the customized quadcopter.

It can be envisioned that both the duration and robustness of a quadcopter can be amplified through solar harvesting capabilities and advanced control strategies based on precise modeling. However, with the addition of these capabilities, further design constraints are applied to an already complex system, such as weight, power, and structural constraints. While the additional design constraints can be difficult to handle, an even larger issue is the modeling and control of the solar-powered quadcopter. Previous quadcopter models assume that when considering drag forces, the shape of the quadcopter can be simplified as a flat plate or blunt body. The lift force generated by the body is generally ignored, as most quadcopters are compact. For a quadcopter with the dimensions presented in this work, not only is the drag force not equivalent to a flat plate, due to turbulence generated by the solar panel and landing gear, the lift generated by the body is non-negligible. In order to accurately incorporate the aerodynamic effects, a computational fluid dynamics model is generated based on the proposed quadcopter design. These aerodynamic effects are then applied to the dynamics model

Logan Towers, Yue Zu, Yen-Chen Liu, Briana Staheli, Yusuke Katagiri, and Samuel Cook are with the Aerospace Engineering Department, Iowa State University, Ames, IA. Emails: `latowers, yzu, clarkliu, bstaheli, katagiri,` and `pscook@iastate.edu`.
Nathaniel Kingly, Yuchen Wang and Ran Dai are with the Mechanical and Aerospace Engineering Department, The Ohio State University, Columbus, Ohio. Emails: `kingry.4, wang.9298` and `dai.490@osu.edu`.

of a quadcopter so that a tuned PID controller can be created that allows the solar-powered quadcopter proposed to fly in a wide range of weather conditions.

The organization of the paper is as follows. The proposed vehicle design is introduced in §II, followed by the development of the quadcopter dynamics model in §III. We then develop a PID controller for stability control under disturbance with simulation verification in §IV. Conclusions with final remarks are addressed in §V.

II. DESIGN AND ESSENTIAL COMPONENTS OF A SOLAR-POWERED QUADCOPTER

A. Energy Consumption and Harvesting Models

Consider a quadcopter equipped with solar cells, allowing it to harvest ambient energy from the environment, that must be capable of carrying a range of sensory equipment, as well as, the needed electronics for efficient solar harvesting. To simplify the analysis of flight performance and capabilities, the energy consumption model is determined under loitering or hovering status. In the case of hovering, the total power consumption is defined as

$$P_{Total,out} = \frac{P_{hover}}{\eta_{motor}} + P_{avionics} + P_{payload}, \quad (1)$$

where the required power for hovering flight is $\frac{P_{hover}}{\eta_{motor}}$ with η_{motor} representing the total electrical efficiency of the system (propeller, motor, and controller efficiencies), $P_{avionics}$ is the power consumed by the avionics system, and $P_{payload}$ represents the power consumed by the sensors. $P_{avionics}$ and $P_{payload}$ are assumed to be constant and insignificant. For a quadcopter with four rotors, the power output can be estimated using the momentum theory and expressed as

$$P_{hover} = \frac{T_{hover}^{3/2}}{\sqrt{2\rho A}}, \quad (2)$$

where $T_{hover} = W$ is the required thrust, which is equal to the weight, to hover, ρ is the air density, and A is the total area of all rotors.

The input power is dependent upon the solar panels. It can be recognized that the energy harvested from the solar panels is a function of the exposed solar cell area, the total efficiency of the energy harvesting system (combined efficiency of the solar cells and the Maximum Power Point Tracking (MPPT) controllers), and the incidence angle of the Sun's rays on the surface of the solar cells. Mathematically, the input power is expressed as

$$P_{solar} = I_E A_s cos(\theta_i)\eta_s \eta_{mppt}, \quad (3)$$

where I_E is the solar insolation that is available on a plane horizontal to the Earth's surface, A_s is the area of the solar panel, θ_i is the angle of incidence between the normal vectors of the sunlight and the solar panel, and η_s and η_{mppt} are the efficiencies of the solar panel and MPPT, respectfully.

Given the power input and output models, in order to maximize the flight time, it is required to optimize the following parameters: power consumption of the motors, which consists of (1) the area of the propellers, (2) motor efficiency, (3) the weight of the system, and the power input of the solar panels, which consists of (4) the area of the solar panels, (5) the efficiency of the cells and MPPT, and (6) the flight location and time.

B. System Overview

Based on the analysis of the solar-powered quadcopter system, the prototype developed attempted to maximize the flight time by examining the six major characteristics described above. Table I provides an overview of the components that has been used in the prototype, where the computer hardware mass includes electronic speed controller (ESC), PixHawk 2 flight controller [19], GPS, MPPT, and all wirings. The propulsion mass includes propellers and motors. The structure mass includes support beams, base plates, motor mounts, clamps, fasteners, and solar panel platform. The solar panel mass includes solar cells and encapsulation.

TABLE I: Specifications of the prototype quadcopter

Component	Value	Unit
Computer hardware mass	0.440	kg
Propulsion mass	1.464	kg
Structural mass	1.967	kg
Solar panel mass	1.200	kg
Battery weight	1.974	kg
Total mass	7.045	kg
Solar panel area	1.375	m^2
Propeller diameter	0.762	m
Overall length and width	2	m
Overall height	0.21	m
Endurance (0.2 kg payload)	2.056	hr
Endurance (max payload)	0.835	hr
Battery type	6S	Li-Ion
Total battery capacity	23800	mAh

Given the incorporation of the solar panels into the quadcopter system, a modified system architecture is used, as seen in Fig 1. While a traditional quadcopter would have the battery directly connected into the power distribution board, in the proposed design the solar panels and battery are both first connected to two MPPTs. These MPPTs manage the selection of the power source. Power is first pulled from the solar panels, if this is not enough to maintain operation then the battery is used. However, if there is excess power then the battery will be charged. In order to monitor the states of the power consumption/harvesting, three voltage/current (V/C) sensors are used. Finally, a traditional power distribution board is used to supply power to the remaining electronics and hardware.
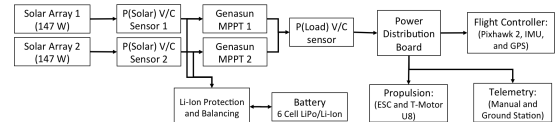

Fig. 1: Solar-powered quadcopter system architecture

Knowing the system characteristics listed in Table I and further discussed below, a performance analysis of the system can be performed. As was discussed earlier, the amount of input power from the solar panels will change based upon the time of year, time of day, and latitude/longitude of the flight. For this analysis, the latitude and longitude was taken to be

Columbus, Ohio, and it was assumed the quadcopter was loitering and carrying a small payload of 0.2 kg. Predicted flight times is shown in Fig. 2.
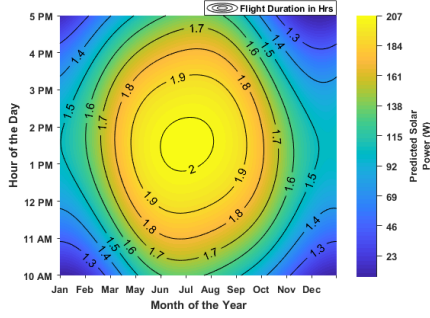

Fig. 2: Flight time analysis through a year at various time of a day based on the prototype quadcopter in Table I

C. Solar Panel Design

Within the system of the solar-powered quadcopter, the two major components that can be optimized via component selection are the solar cells and the MPPT. Currently, there are a wide range of cells that can be used such as mono crystalline silicon (15-20%), polycrystalline silicon (13-16%), thin-film (7-13%), and amorphous silicon (6-8%) [20].

In terms of selecting a solar cell for a quadcopter, the key factor is efficiency. For this reason, it was selected to use SunPower C60 solar cells. Each cell has the electrical properties outlined in Table II under standard testing conditions (STC), which are a cell temperature of $25°C$ and an irradiance of $1000 \ W/m^2$ with an air mass 1.5 (AM1.5), where AM is a measure of the length of the atmosphere solar radiation encounters before reaching the surface. These conditions are defined by ASTM G173 [21].

TABLE II: Electrical properties of SunPower C60 cells [22]

P_{mpp} (W$_P$)	Efficiency (%)	V_{mpp} (V)	I_{mpp} (A)	V_{oc} (V)	I_{sc} (A)
3.34	21.8	0.574	5.83	0.682	6.24

To charge the onboard battery (22.2 V nominal), 44 pieces of SunPower C60 solar cells with each one at the dimension of 12.5×12.5 cm^2 are placed in series to create a single solar panel. Due to the power requirements and goal of extending the flight duration, it was selected to incorporate two sets of these panels for a total of 88 pieces of SunPower C60 solar cells, which require an area of 1.375 m^2 and provide 293.92 W of power in STC.

D. Propulsion Analysis

The motor selection process for the prototype is particularly challenging due to the weight and power restrictions the solar array imposed on the system. Opting to use a Lithium-Ion battery for its energy density (243 Wh/Kg) placed additional limitations on the motor selection. For the selected battery configuration, the current draw was limited to 47.6 A maximum. With this in mind, the T-motor U8 was used as it offers high thrust characteristics, allows for the use of a large propeller diameter and high electrical and thrust

efficiencies. The characteristics of the T-Motor U8 and the 0.762 m diameter propeller used for the prototype are listed in Table III.

TABLE III: T-Motor U8 100 KV Motor Specifications

Throttle (%)	Current (A)	Power (W)	Thrust (N)	Efficiency (N/W)
50	2.1	46.62	9.582	0.206
65	3.3	73.26	12.78	0.174
75	5.5	122.1	18.97	0.155
85	6.7	148.7	22.07	0.148
100	8.3	184.3	26.61	0.144

E. Structure Composition

The structure of the prototype was designed to minimize the amount of unnecessary components. The structure of the quadcopter, as shown in Fig. 3, consists of three carbon fiber tubes aligned in an 'x' configuration attached to carbon fiber center plates. The motors are attached to the carbon fiber tubes by carbon fiber plates and aluminum clamps. The spacing between center plates is for the electrical components. The solar panel plate, which supplements for the lack of rigidity and structural stability of the fragile SunPower C60 solar cells, is a carbon fiber sandwich with Nomex honeycomb core to reduce weight.

Fig. 3: A prototype of customized solar-powered quadcopter

III. MODEL CONSTRUCTION

A. Flight Dynamics Model

In this section, a mathematical model of the quadcopter flight dynamics is developed. The schematic diagram of the quadcopter is shown in Fig. 4, where **B** denotes body fixed frame and **E** denotes inertial frame. The linear position of the quadcopter is defined as $\bar{\xi} = (x, y, z)^{\mathrm{T}}$ and three Euler angles are defined as $\bar{\eta} = (\phi, \theta, \psi)^{\mathrm{T}}$. As shown in Fig. 4, roll, pitch, and yaw angles represent rotation angles around x, y and z axis, respectively. Note that the quadcopter has four motors with two spinning clockwise and the others spinning counter-clockwise, so that the torque generated is negated. By controlling the speed of each rotor (Ω_{1-4}), altitude and attitude of a quadcopter can be controlled.
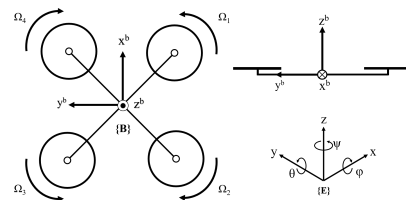

Fig. 4: A schematic diagram of a quadcopter.

Developing the flight dynamics model of the solar-powered quadcopter is based on a set of assumptions, including rigid and symmetrical structure of the quadcopter, coincidence of the center of gravity and origin of the body fixed frame, proportional relationships between the thrust/drag torques and the square of rotor speed, and rigid propellers [23]. From Newton-Euler equations and Newton's second law, the flight dynamics model of a quadcopter is derived as follows [24],

$$\ddot{x} = \frac{U_1(cos\psi sin\theta cos\phi + sin\psi sin\phi)}{m} \tag{4}$$

$$\ddot{y} = \frac{U_1(sin\psi sin\theta cos\phi - cos\psi sin\phi)}{m} \tag{5}$$

$$\ddot{z} = \frac{U_1(cos\theta cos\phi)}{m} - g \tag{6}$$

$$\ddot{\phi} = \frac{\dot{\theta}\dot{\psi}(I_y - I_z) - J_r\dot{\theta}\Omega_r + \frac{U_2 l}{\sqrt{2}}}{I_x} \tag{7}$$

$$\ddot{\theta} = \frac{\dot{\phi}\dot{\psi}(I_z - I_x) - J_r\dot{\phi}\Omega_r + \frac{U_3 l}{\sqrt{2}}}{I_y} \tag{8}$$

$$\ddot{\psi} = \frac{\dot{\phi}\dot{\theta}(I_x - I_y) + U_4}{I_z} \tag{9}$$

where m is the mass of the quadcopter, l is the distance between the rotor axis and the center of gravity of the quadcopter, I_x, I_y, I_z are the moments of inertia about the x, y and z axis, respectively, J_r is the rotor's moment of inertia, and the disturbance is denoted by $\Omega_r = \Omega_4 + \Omega_2 - \Omega_1 - \Omega_3$. U_1 to U_4 represent control inputs of 4 rotors, which are determined by

$$\begin{bmatrix} U_1 \\ U_2 \\ U_3 \\ U_4 \end{bmatrix} = \begin{bmatrix} b & b & b & b \\ -b & -b & b & b \\ -b & b & b & -b \\ -d & d & -d & d \end{bmatrix} \begin{bmatrix} \Omega_1{}^2 \\ \Omega_2{}^2 \\ \Omega_3{}^2 \\ \Omega_4{}^2 \end{bmatrix}, \tag{10}$$

where b and d are thrust and drag (moment) constants of the rotors.

In order to develop an accurate mathematical model of the developed quadcopter, the relationship between the motor revolutions per minute (RPM) and thrust/torque (b and d) needed to be determined. This was accomplished through experimental testing of the motors and propellers to establish the relationship between Ω_{1-4} and U_{1-4}. These tests were completed by attaching the motor to a test stand that was connected to two vernier dual-range force sensors [25]. Each motor/propeller pair was then slowly throttled from 0-100% with the thrust and torque simultaneously. The RPM was determined from the ESC. A desired control input set $[U_1, U_2, U_3, U_4]^T$ can be achieved by setting corresponding rotor speed from the following relationship,

$$\begin{bmatrix} \Omega_1{}^2 \\ \Omega_2{}^2 \\ \Omega_3{}^2 \\ \Omega_4{}^2 \end{bmatrix} = \frac{1}{4} \begin{bmatrix} b & -b & -b & -d \\ b & -b & b & d \\ b & b & b & -d \\ b & b & -b & d \end{bmatrix} \begin{bmatrix} U_1 \\ U_2 \\ U_3 \\ U_4 \end{bmatrix}. \tag{11}$$

B. Computational Fluid Dynamics (CFD) Model

The quadcopter flight dynamics model is an ideal one without considering any external disturbances. However, in real-world scenarios there are many environmental factors that could generate external forces. The major external force is the wind force acting on the body that generates drag and lift forces. The effects of a quadcopter flying in a wind field has been described in [17]. Due to the significantly extended scale of the solar-powered quadcopter body prescribed in §II, we focus on the aerodynamic effects of the quadcopter body, while ignoring the propeller effects. Existing work in [17], [26] assumes the lift generated by a quadcopter is negligible and shape of the body that receives the drag can be simplified as a flat plate. Due to the size of the developed prototype, we performed thorough analysis of the lift coefficient, as well as, the drag coefficient. Per the above discussion, the aerodynamic effects will be integrated into the flight dynamics model in (4)-(6) by adding the disturbances term $\bar{F}_d = [F_x, F_y, F_z]^T$, expressed as

$$\ddot{x} = \frac{U_1(cos\psi sin\theta cos\phi + sin\psi sin\phi) - F_x}{m}$$
$$\ddot{y} = \frac{U_1(sin\psi sin\theta cos\phi - cos\psi sin\phi) - F_y}{m} \tag{12}$$
$$\ddot{z} = \frac{U_1(cos\theta cos\phi) + F_z}{m} - g.$$

The disturbance forces generated by wind is determined by

$$F_x = \frac{1}{2}C_d\rho V_{wx}^2 A$$
$$F_y = \frac{1}{2}C_d\rho V_{wy}^2 A, \tag{13}$$
$$F_z = \frac{1}{2}C_l\rho(V_{wx}^2 + V_{wy}^2)A,$$

where $\bar{V}_w = [V_{wx}, V_{wy}, V_{wz}]^T$ is the wind speed, C_d is the drag coefficient, C_l is the lift coefficient, and A is the reference surface area over which the air flows.

In order to accurately predict the flight performance of the solar-powered quadcopter, a CFD simulation is applied to acquire the aerodynamic characteristics. The properties of objective model can be further observed from the reactions of fluid flows in the numerical experiment. In this work, a three dimensional physical condition is simulated with the full-scale geometry of the vehicle via STAR CCM+ software. The three-dimensional model, generated in SolidWorks, is imported to simulate the lift and drag coefficient for the quadcopter at various angles of attack using K-Epsilon Two-Layer Turbulence Model, as shown in Fig. 5 (a), with the arm supports removed to allow for higher resolution mesh on the propellers.

To understand the propellers interaction with the solar panel plate, the simulation reconstructs the hovering condition by assuming that all propellers are rotating. Four cylindrical regions are created for each propeller, as shown Fig. 5 (b). To simulate the wind effects, the quadcopter is placed in a control volume (29.9x13.8x4 m), as demonstrated in Fig. 5 (c). The boundary conditions are defined as a

velocity inlet equal to 5 m/s and a pressure outlet with standard atmospheric pressure. Based on the motor test, the rotational speed of each propeller is set to 1550 RPM. The resulting mesh from the surface remesher, automatic surface repair, trimmer cell mesher, and prism layer mesh is demonstrated in Fig. 5 (d).
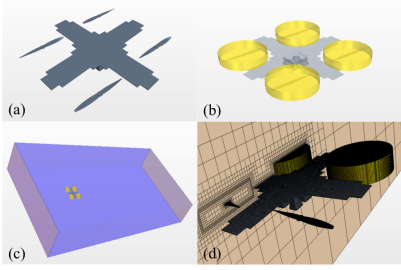

Fig. 5: CFD simulation settings

To validate the simulation, the torque produced by each propeller was monitored and compared to the motor/propeller testing results. In the simulation, each propeller exerted a torque of 2.5179 ± 0.07934 Nm, where as in the motor tests, each motor/propeller pair exerted a torque of 2.5365 ± 0.10423 Nm.

Finally, using the forces acting on the z-axis (lift) and x-axis (drag), the aerodynamic characteristics C_l and C_d of the proposed quadcopter can be determined. Based on the assumption that the quadcopter will not fly at high angles of attack, simulations were conducted at various angles of attack from $0°$ to $10°$. The results from the simulations using Ohio State University Supercomputer Resources [27] are shown in Fig. 6. From these results, multiple important characteristics can be determined, including the deviation from flat plate aerodynamics, optimal flight angle, and the significance of the wind effect on the quadcopter.
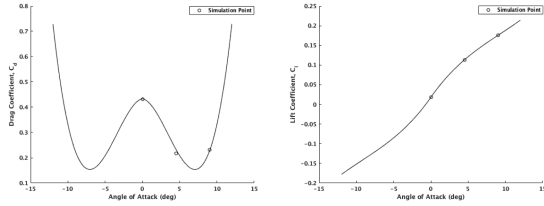

Fig. 6: C_d (left) and C_l (right) vs Angle of Attack

Compared to the aerodynamics of a flat plate in Fig. 8, the CFD simulation results indicate that the C_d of the model presented in this paper does not follow the trend of a flat plate. The reason for this inconsistency is the turbulent flow caused by the winds interaction with the quadcopter's solar panel platform and landing gears. This effect is reduced as angle of attack is increased and less of the landing gears come in contact with the freestream flow. The generated turbulence in the STAR CCM+ simulations is shown in Fig. 7.

While the quadcopter structure was not designed for aerodynamic efficiency, due to the size of the structure the lift produced is not negligible. By examining the lift to drag ratio (L/D), one can determine a potential optimal flight angle, which occurs at the maximum L/D. This is shown in Fig. 8,
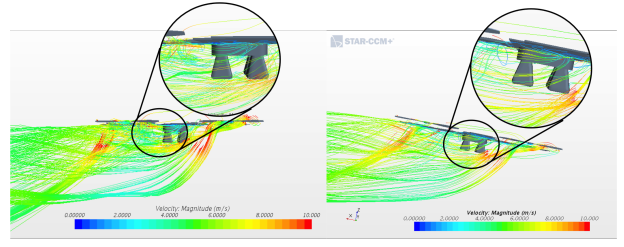

Fig. 7: CFD simulation with streamline flow at $0°$ (left) and $4.5°$ (right) angle of attack

where the maximum L/D is approximately 1 and the angle of attack at this point is $7.4°$.
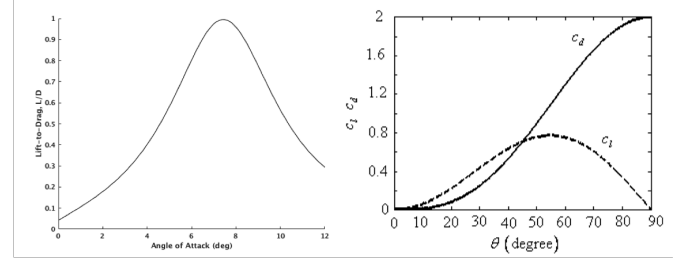

Fig. 8: Lift to drag ratio (left) and aerodynamics of a flat plate [28] (right)

Lastly, it is important to understand to what degree the wind effects can impact the flight stability of the quadcopter. First, an analysis of the lift and drag forces created by various wind conditions $(0 - 10$ m/s$)$ and flight angles $(0 - 12°)$ was conducted. In order to statistically substantiate the forces produced, an analysis of the quadcopter in hovering conditions was performed. The average and standard deviation was determined to be 16.16 N ± 0.2873 N. Using a 3-sigma bound on the hovering condition as a measure of statistical significance, the lift and drag forces can be deemed statistically significant if they are greater than 0.862 N or about 5%. This analysis can be seen in Fig. 9, where the dark blue regions show regions of insignificance of lift/drag forces, while colored regions depict regions of significance of lift/drag forces.
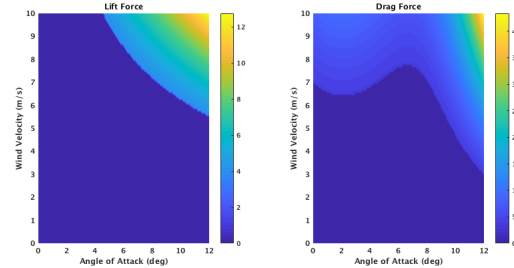

Fig. 9: Significance of lift (left) and drag (right) forces

IV. CONTROLLER DESIGN AND SIMULATION VERIFICATION

A. PID Controller Design

In this section, PID controllers for controlling the quadcopter position and attitude are designed and implemented in Simulink, shown in Fig. 10, for verification. PID controllers

are widely used in industry for a variety of control objects due to their simple implementation and high performance [29].
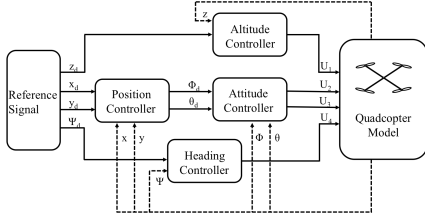

Fig. 10: Block diagram of the feedback control system simulation model

Let $\bar{\xi}_d = [x_d, y_d, z_d]^{\mathrm{T}}$ denote the desired position and $\bar{\eta}_d = [\phi_d, \theta_d, \psi_d]^{\mathrm{T}}$ denote the desired attitude angles. In general cases, the objective of stability control is to guide the quadcopter to transport from current state to a desired state, $[x_d, y_d, z_d, \psi_d]$, and then maintaining the hovering status with $\phi_d = 0$, $\theta_d = 0$. The desired position accelerations, $\ddot{x}_d$, $\ddot{y}_d$ and $\ddot{z}$, and attitude accelerations $\ddot{\phi}_d$, $\ddot{\theta}_d$ and $\ddot{\psi}_d$, are obtained using PID controllers, which are similarly found as [30],

$$\ddot{x}_d = K_p^x(x_d - x) + K_d^x(\dot{x}_d - \dot{x}) + K_i^x \int (x_d - x)dt, \quad (14)$$

where $K_p^\bullet$, $K_d^\bullet$, and $K_i^\bullet$ denote proportional gain, derivative gain, and integral gain for variable '$\bullet$', respectively. From the PID controllers, the desired values of U_1 to U_4 can be obtained from (4)-(9) and the real control inputs can be achieved by adjusting the thrust and drag (moment) constants of the rotors in (10).

Under the hovering conditions, the rotational angles, ϕ and θ, are assumed to be small, hence $\ddot{x}$ and $\ddot{y}$ in (12) can be simplified as

$$\begin{bmatrix} \ddot{x}_d \\ \ddot{y}_d \end{bmatrix} = \frac{U_1}{m} \begin{bmatrix} sin\psi & cos\psi \\ -cos\psi & sin\psi \end{bmatrix} \begin{bmatrix} \phi_d \\ \theta_d \end{bmatrix} - \begin{bmatrix} F_x/m \\ F_y/m \end{bmatrix}. \quad (15)$$

From the above equations, the desired roll and pitch angles can be derived and written as

$$\begin{bmatrix} \phi_d \\ \theta_d \end{bmatrix} = \frac{m}{U_1} \begin{bmatrix} sin\psi & -cos\psi \\ cos\psi & sin\psi \end{bmatrix} \begin{bmatrix} \ddot{x}_d + F_x/m \\ \ddot{y}_d + F_y/m \end{bmatrix}, \quad (16)$$

which are used to obtain the desired roll and pitch angles.

B. Simulation Results

In this section, simulation examples are implemented using the above designed feedback control system based on the flight and disturbances model in §IV. The wind effect is assumed as a trapezoidal waveform, as shown in Fig. 11. For the simulations, the vertical component of the wind is set to zero since it induces limited influence compared to the horizontal components in terms of the horizontal position and attitude controller, which is the focus of this control design. The peak wind speed is 5 m/s along the x axis and 6 m/s along the y axis. Moreover, wind noise is considered, which adds a Gaussian distribution with a mean of 0 m/s and a standard deviation of 0.1 m/s, which allows a maximum deviation of approximately ± 0.5 m/s. The quadcopter starts at a position $[x, y, z] = [0, 0, 0]$ m with a pose angle of

$[\phi, \theta, \psi] = [0, 0, \pi]$. The goal is to hover at a final position of $[x, y, z] = [1, 1, 5]$ m. Parameters used in the simulation example are listed in Table IV.
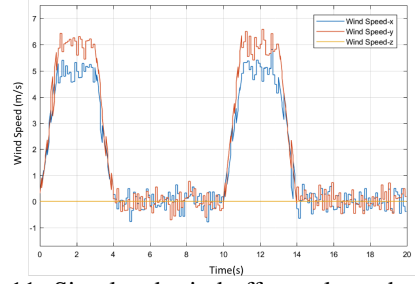

Fig. 11: Simulated wind effects along three axis.

TABLE IV: Simulation parameter values

Parameter	Value	Unit
I_x	1.05	kgm^2
I_y	1.05	kgm^2
I_z	2.05	kgm^2
m	6.77	kg
g	9.81	m/s^2
l	0.915	m
b	1.74e-4	Ns^2
d	9.80e-5	Nms^2

The APM Planner 2 integrated with Pixhawk2 is used to control the motion of the quadcopter. To be consistent with the feedback model settings provided by the APM Planner 2 interface, the original PID controller is reduced to a PID/PI combined controller, i.e., PI for horizontal displacement control and PID for the remaining variables. There are many methods for PID gain tuning, such as trial and error, Ziegler-Nichols method, and etc. We adopt the trial and error method. Accordingly, the designed PID/PI gains are illustrated in Table V. In order to efficiently tune the gains, we consider all three types of settings provided by the APM Planner 2 interface, including altitude hold, rate control and throttle acceleration control. For the Pixhawk2, the altitude hold controller operates as an outer loop with the rate and throttle acceleration controllers as inner loops. It is because of this hierarchical control structure that causes the altitude hold controller to be pure proportional control, as it only determines desired positions/attitudes to the inner loop.

TABLE V: PID controller gains

	K_p	K_i	K_d
Altitude Hold			
x	1	N/A	N/A
y	1	N/A	N/A
z	1	N/A	N/A
ϕ, θ, ψ	5	N/A	N/A
Rate (Velocity) Control			
$\dot{x}$	2	1	N/A
$\dot{y}$	2	1	N/A
$\dot{z}$	5	N/A	N/A
$\dot{\phi}, \dot{\theta}, \dot{\psi}$	1	1	20
Throttle Acceleration Control			
$\ddot{z}$	4	1	2

To demonstrate the advantages of precise modeling when accounting for aerodynamic effects in stability control of the prototype quadcopter, three types of models are used in

simulations performed. The first, actual model with feedback, generates controls incorporating the precise aerodynamic model built in §III.B. The second, flat plate model with feedback, generates controls considering the aerodynamic model of a flat plate. Lastly, a third, actual model without feedback, does not account for the aerodynamic effects. All simulation cases last for 20 seconds and use a sample rate of 20 Hz. During this time interval, the time histories of position and attitude of the quadcopter are shown in Fig.12.

In all three simulation cases, the quadcopter reaches at the desired position within 8 seconds and remains at a stable status when there is no wind disturbance. Under wind disturbances, a tuned PID controller with precise aerodynamic models leads to reduced deviation and faster response. The amplified plots in Fig.12 demonstrate the improved stability under disturbances for a controller with precise estimation of the aerodynamic effects. Moreover, the simulation results verify the feasibility of using the designed PID/PI gains from Table V in real flight, which is further verified in the following section.

C. Flight Tests

In order to verify the flight characteristics and the capabilities of the proposed design, a demonstrator was built and flight tests were conducted. This demonstrator has the same characteristics as the proposed design, however, uses a Lithium-Polymer battery, a fiber glass/nomex composite solar panel structure plate, and non-optimized electronic hardware and motor mounting brackets. These items were used because of availability, limited budget, and other constraints. The total weight of the demonstrator and other characteristics are listed below in Table VI. Compared to the optimized designed weight (7.045 kg) in Table I, the demonstrator weighs an extra 1.13 kg due to the construction constraints.

TABLE VI: Specifications of the demonstrator quadcopter

Component	Value	Unit
Computer hardware mass	0.440	kg
Propulsion mass	1.464	kg
Structural mass	4.055	kg
Solar panel mass	1.200	kg
Battery weight	0.769	kg
Total mass	8.175	kg
Battery type	6S	Li-Po
Total battery capacity	6600	mAh

Given this demonstrator, multiple flight tests were conducted. The first set of flights were conducted using only a lithium polymer battery as the power source with the with the solar panel mass, consisting of the solar cells and encapsulation removed. These tests show the stability of the quadcopter with weight and power consumption consistent with the presented design in §II, while maintaining the same susceptibility to wind effects. For comparison, the demonstrator without the solar panel mass weighs 6.975 kg while the presented design weighs 7.045 kg. These flights took place at the Aerospace Research Center (ARC) located at The Ohio State University airport (KOSU) on September 8, 2017 at 11 am. It was a clear sky at $64.9°$ F and 4.6 mph variable

winds. Figure 13 shows the power consumption along with the attitude of the quadcopter over the duration of one of the flights. The average current draw was 4.9 Amps per motor, which is consistent with the predicted flight times discussed in §II. It also indicates with the proposed components we will achieve the desired flight duration indicated in Table I.
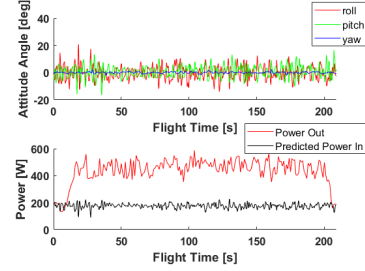

Fig. 13: Flight Data from Demonstrator Flight with no Solar Panels.

The next set of flights conducted with the solar panel mass included, which allowed the power source to be a combination of the lithium polymer battery and solar panels. This verifies the solar-energy harvesting capabilities while in flight. This flight took place at the ARC at KOSU on September 10, 2017 at noon. It was mostly clear skies with a very thin cloud cover at $64.0°$ F and 8.1 mph winds. Fig. 14 demonstrates the power consumption, power harvested, and attitude of the quadcopter over the duration of the flight. In Fig. 14, there is a small deviation between the predicted and experimental power in of roughly 5%. This minor difference can be attributed to the thin cloud cover, which is not estimated in the prediction model. Video clips of the flight test series are also included with explanations. The demonstrator with solar panels attached adds 1.2 kg payloads, which increases the average current draw to 7.25 Amps per motor and reduced the flight duration to approximately 1 hour. As discussed above, to obtain the predicted flight duration in Table I, the next generation demonstrator will integrate optimized components to reduce the quadcopter weight.
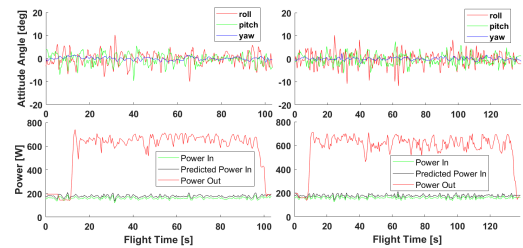

Fig. 14: Flight Data from two demonstrator flights with Solar Panels.

V. CONCLUSION

This paper presents the design, modeling, and control of a solar-powered quadcopter that leads to significant extended flight duration with payload capacities. Both flight dynamics and aerodynamics models of the quadcopter are developed. Further analysis of the aerodynamics effects on the customized solar-powered quadcopter demonstrates that the shape of the quadcopter cannot be simplified as a flat
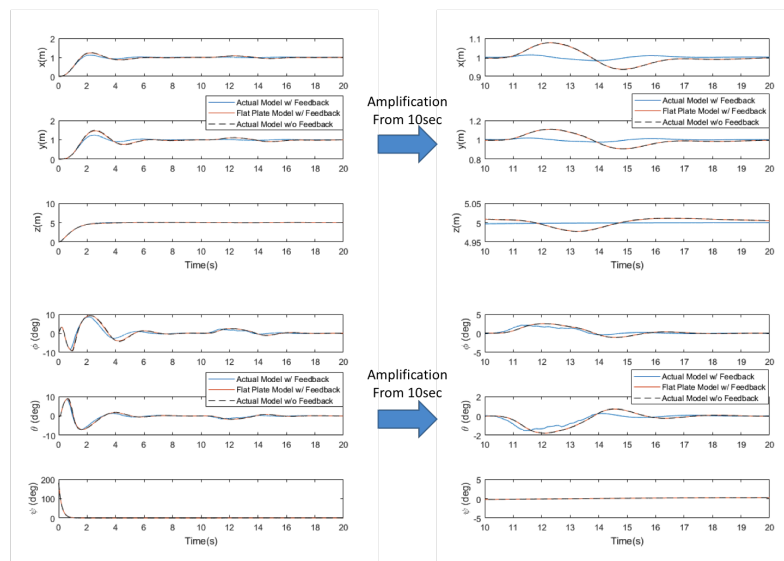
Fig. 12: Simulation results of displacements & attitude from three types of controllers.

plate when determining aerodynamic characteristic parameters. PID controllers for stability control of the solar-powered quadcopter under wind disturbances are developed and verified through MATLAB/Simulink simulations and real-world flight tests. Future work will further optimize the design based upon the knowledge gained in flight test, integrate the weight reductions, and perform extensive outdoor, solar-powered flight tests.

REFERENCES

[1] S. Gupte, P. I. T. Mohandas, and J. M. Conrad, "A survey of quadrotor unmanned aerial vehicles," in *Southeastcon, 2012 Proceedings of IEEE*, 2012, pp. 1–6.

[2] D. J. Pines and F. Bohorquez, "Challenges facing future micro-air-vehicle development," *Journal of aircraft*, vol. 43, no. 2, pp. 290–305, 2006.

[3] (2016) Dji phantom 4 pro. [Online]. Available: http://www.dji.com/phantom-4-pro

[4] N. K. Ure, G. Chowdhary, T. Toksoz, J. P. How, M. A. Vavrina, and J. Vian, "An automated battery management system to enable persistent missions with multiple aerial vehicles," *IEEE/ASME Transactions on Mechatronics*, vol. 20, no. 1, pp. 275–286, 2015.

[5] S. Nebiker, A. Annen, M. Scherrer, and D. Oesch, "A light-weight multispectral sensor for micro uavopportunities for very high resolution airborne remote sensing," *The international archives of the photogrammetry, remote sensing and spatial information sciences*, vol. 37, no. Vi, pp. 1193–1200, 2008.

[6] J. S. Gadda and R. D. Patil, "Quadcopter (uavs) for border security with gui system," *International Journal of Engineering Research and Technology*, vol. 2, no. 12, pp. 620–624, 2013.

[7] N. Bezzo, K. Mohta, C. Nowzari, I. Lee, V. Kumar, and G. Pappas, "Online planning for energy-efficient and disturbance-aware uav operations," in *Intelligent Robots and Systems (IROS), 2016 IEEE/RSJ International Conference on*. IEEE, 2016, pp. 5027–5033.

[8] J. Verbeke, D. Hulens, H. Ramon, T. Goedeme, and J. De Schutter, "The design and construction of a high endurance hexacopter suited for narrow corridors," in *International Conference on Unmanned Aircraft Systems (ICUAS)*, 2014.

[9] T. Pang, K. Peng, F. Lin, and B. M. Chen, "Towards long-endurance flight: Design and implementation of a variable-pitch gasoline-engine quadrotor," in *12th IEEE International Conference on Control and Automation (ICCA)*, 2016.

[10] R. Sowah, M. A. Acquah, A. R. Ofoli, G. A. Mills, and K. M. Koumadi, "Rotational energy harvesting to prolong flight duration of quadcopters," in *Industry Applications Society Annual Meeting*. IEEE, 2015.

[11] M. C. Achtelik, J. Stumpf, D. Gurdan, and K.-M. Doth, "Design of a flexible high performance quadcopter platform breaking the mav endurance record with laser power beaming," in *International Conference on Intelligent Robots and Systems (IROS)*, 2011.

[12] M. H. Shaheed, A. Abidali, J. Ahmed, S. Ahmed, I. Burba, P. J. Fani, G. Kwofie, K. Wojewoda, and A. Munjiza, "Flying by the sun only: The solarcopter prototype," *Aerospace Science and Technology*, vol. 45, pp. 209–214, 2015.

[13] J. Borenstein, "The hoverbot - an electrically powered flying robot," 1992, unpublished paper, University of Michigan. [Online]. Available: http://ftp.eecs.umich.edu/people/johannb/paper99.pdf

[14] E. Nice, "Design of a four rotor hovering vehicle," Ph.D. dissertation, Cornell University, 2004.

[15] P. Pounds and R. Mahony, "Design principles of large quadrotors for practical applications," in *IEEE International Conference on Robotics and Automation (ICRA)*, 2009.

[16] A. Bemporad, C. A. Pascucci, and C. Rocchi, "Hierarchical and hybrid model predictive control of quadcopter air vehicles," *IFAC Proceedings Volumes*, vol. 42, no. 17, pp. 14–19, 2009.

[17] N. K. Tran, E. Bulka, and M. Nahon, "Quadrotor control in a wind field," in *Unmanned Aircraft Systems (ICUAS), 2015 International Conference on*. IEEE, 2015.

[18] I.-Y. Ahn, J.-S. Bae, S. Park, and Y.-M. Yang, "Development and flight test of a small solar powered uav," *Journal of the Korean Society for Aeronautical & Space Sciences*, vol. 41, no. 11, pp. 908–914, 2013.

[19] "Pixhawk2.1," 2017. [Online]. Available: http://www.proficnc.com/

[20] M. A. Green, K. Emery, Y. Hishikawa, W. Warta, and E. D. Dunlop, "Solar cell efficiency tables (version 45)," *Progress in photovoltaics: research and applications*, vol. 23, no. 1, pp. 1–9, 2015.

[21] G. Committee *et al.*, "Tables for reference solar spectral irradiances: Direct normal and hemispherical on 37 tilted surface," *ASTM International*, 2012.

[22] SunPower. (2017) C60 solar cell mono crystalline silicon. [Online]. Available: http://us.sunpowercorp.com/

[23] H. Bolandi, M. Rezaei, and R. Mohsenipour, "Attitude Control of a Quadrotor with Optimized PID Controller," *Intelligent Control and Automation*, pp. 335–342, 2013.

[24] J. Li and Y. Li, "Dynamic analysis and PID control for a quadrotor," *2011 IEEE International Conference on Mechatronics and Automation*, pp. 573–578, 2011.

[25] (2016) Dual-range force sensor. [Online]. Available: http://www.vernier.com/products/sensors/force-sensors/dfs-bta/s

[26] M. Fatan, B. L. Sefidgari, and A. V. Barenji, "An adaptive neuro pid for controlling the altitude of quadcopter robot," in *Methods and models in automation and robotics (mmar), 18th international conference on*, 2013.

[27] O. S. Center, "Ohio supercomputer center," http://osc.edu/ark:/19495/f5s1ph73, 1987.

[28] NPTEL. (2016) Compressible flow. [Online]. Available: http://nptel.ac.in/courses/101103004/module4/lec8/3.html

[29] R. Toscano, "A simple robust PI/PID controller design via numerical optimization approach," *Journal of Process Control*, vol. 15, no. 1, pp. 81–88, 2005.

[30] V. Ghadiok, J. Goldin, and W. Ren, "Autonomous indoor aerial gripping using a quadrotor," *IEEE International Conference on Intelligent Robots and Systems*, pp. 4645–4651, 2011.